Macromolecules

pubs.acs.org/Macromolecules Article

Mapping the Dynamics of Fluctuations and Defects in Confined Block Copolymer Films with High-Speed Atomic Force Microscopy

Julia G. Murphy, Jonathan G. Raybin, and Steven J. Sibener*

Cite This: *Macromolecules* 2024, 57, 7270−7279 Read Online

ACCESS | Metrics & More | Article Recommendations | Supporting Information

ABSTRACT: The application of block copolymer (BCP) templates for nanofabrication is currently limited by structural disorder of the nanoscale pattern. To study pattern fluctuations and defects, we apply high-speed atomic force microscopy to track the dynamics of confined poly(styrene-*block*-methyl methacrylate) cylinders during *in situ* thermal annealing. For this investigation, we use wedge-shaped trenches as a controlled platform for systematically examining the effects of strain and defectivity. By mapping the spatial distribution of domain fluctuations, we identify strong fluctuation enhancement in the vicinity of defect sites. Fluctuations are further influenced by local strain and proximity to the trench sidewalls. To explain these trends, we develop an analytic free-energy model for predicting fluctuations in confined BCP. Finally, we leverage our high-speed imaging to directly track defect healing mechanisms in the confined domains. Altogether, these experiments elucidate the collective interactions of defects, fluctuations, and strain during the assembly and alignment of BCP patterns.

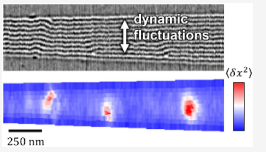

INTRODUCTION

Over the past six decades, advances in computing technology have been largely driven by the miniaturization of transistors, leading to an exponential increase in computing power as described by Moore's law. Continuing this trend, however, will require the development of new nanofabrication strategies that can extend beyond the traditional limitations of top-down photolithography. Bottom-up fabrication through the directed self-assembly (DSA) of block copolymer (BCP) templates has emerged as one promising approach.[1−3] This technique leverages the intrinsic ability of BCPs to self-assemble into highly regular nanopatterns with half-pitch length scales as low as 6−10 nm.[4−6] As a method for controlling the orientation and registration of BCP patterns, DSA is achieved by modifying the underlying substrate with chemical or topographic guides.[7] Despite successful demonstrations on wafer-scale samples,[8,9] improvements in pattern quality are still needed for DSA to be integrated into industrial process flows. Pattern disorder — including line roughness, errors in registration, and morphological defects — remains a limiting factor for these applications.[10−13] Furthermore, researchers often aim to use DSA to prepare irregular template designs that intentionally incorporate defect elements, such as jogs, T-junctions, and bends, for more sophisticated device architectures.[14,15] These objectives underscore the need for improved measurement techniques and deeper understanding of disorder in BCP templates.

Graphoepitaxy, as a specific case of DSA, involves confining BCP in topographic trenches, such that the trench sidewalls act as boundary conditions that enforce pattern alignment.[16,17] When the trench width is incommensurate with the natural domain spacing, confinement introduces strain and leads to an increase in free energy with respect to bulk unconfined samples. The excess confinement free energy may be estimated from the balance between elastic chain stretching and block incompatibility, as first described by Turner[18] and Walton et al.[19] These initial confinement models considered the scenario of well-ordered systems where strain is evenly shared across the confined domains.

In practice, however, BCP patterns are inherently perturbed by internal structural disorder, including both equilibrium composition fluctuations and nonequilibrium defects.[20−22] During annealing, thermal fluctuations serve as an intrinsic source of variability in the alignment of domains as well as the structure and composition of interdomain boundaries.[10] These dynamic fluctuations are preserved as undesired line roughness in static films quenched below the glass transition. Meanwhile, defects, which represent metastable states, disrupt pattern connectivity and arise from kinetic trapping during pattern formation and processing.[23] Both forms of disorder—fluctuations and defects—frustrate chain packing and destabilize the confined BCP system. Understanding and controlling pattern dynamics during assembly is crucial for improving the performance of BCP nanofabrication.

Tracking dynamic phenomena in BCP films requires effective measurement under high-temperature thermal annealing conditions. Electron microscopy, while commonly used for the characterization of thermally quenched BCP structures, is unsuitable for dynamic studies due to sample damage from ionizing radiation. As an alternative, a variety of X-ray and

Received: March 20, 2024
Revised: June 20, 2024
Accepted: July 19, 2024
Published: July 26, 2024

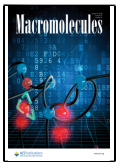

https://doi.org/10.1021/acs.macromol.4c00638
Macromolecules 2024, 57, 7270−7279

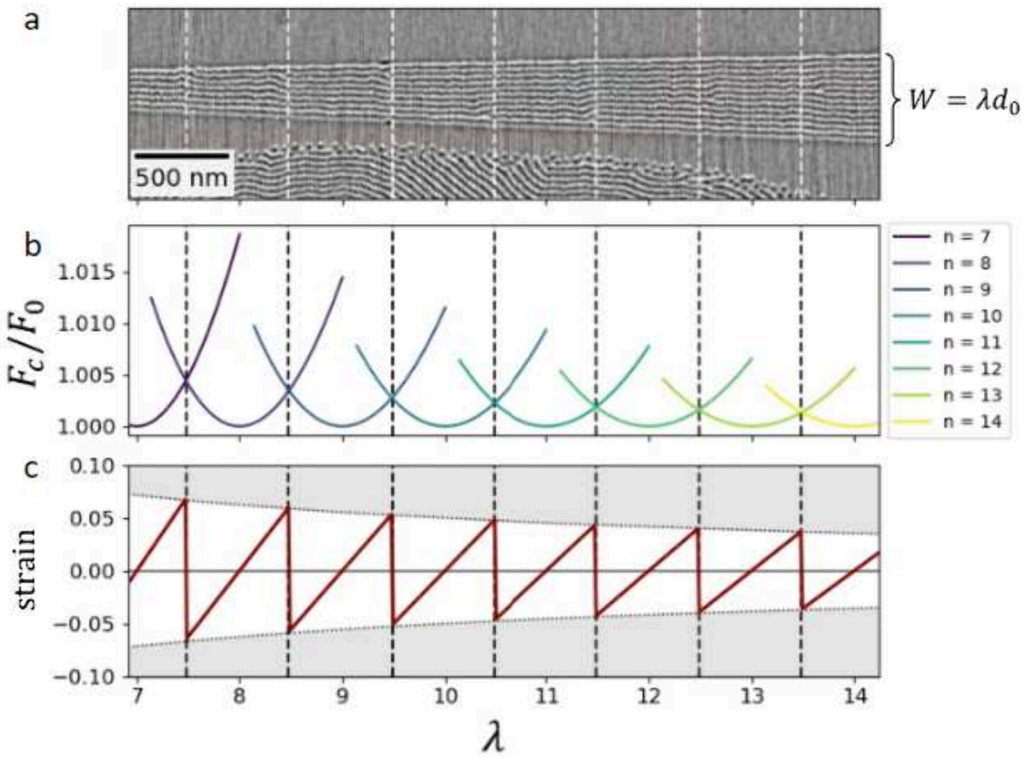

Figure 1. BCP confinement in wedge-shaped trenches. (a) AFM phase image of confined PS-*b*-PMMA in a wedge-shaped trench with continuously varying width W. BCP domains are aligned within the trench and oriented randomly outside the trench. The PS and PMMA domains appear as light and dark stripes, respectively. (b) Plot of the free-energy per chain F_c/F_0 as a function of the reduced trench width $\lambda = W/d_0$. The number of confined domains n changes discontinuously as the trench widens, forming dislocations at equilibrium positions indicated by the dashed vertical lines. (c) Plot of average strain as a function of λ. Strain changes discontinuously at defect sites forming a sawtooth wave, with a peak magnitude bounded by $\pm 1/(2\lambda)$.

neutron scattering methods have enabled *in situ* investigation of the bulk pattern morphology, defectivity, and line roughness of BCP films during thermal annealing.[24,25] In particular, resonant soft X-ray scattering (RSoXS) leverages the native chemical contrast of BCP domains, allowing three-dimensional reconstruction of the through-film morphology.[26] However, these reciprocal space scattering techniques probe the film over a roughly 100 μm spot size and do not provide details on individual defect structures or nanoconfined systems. In contrast, atomic force microscopy (AFM) enables non-destructive nanoscale imaging, but until recently has been limited by slow scan rates that undersample relevant defect interactions. However, with improvements in time resolution of roughly 2 orders of magnitude, the advent of high-speed AFM has provided new opportunities for following BCP pattern dynamics in real space and time.[27] Since its development, high-speed AFM has empowered direct observations of many dynamic phenomena in BCP systems, including domain fluctuations,[28] pattern formation and alignment,[29,30] and terrace nucleation.[31]

Here, we apply high-speed AFM to track fluctuations and defect dynamics in confined BCP cylinders during *in situ* thermal annealing. For this study, we utilize wedge-shaped trenches, following the approach developed by Tong et al.[32] The wedge geometry imposes a continuously varying confinement width that simultaneously samples a range of strain environments, while also introducing dislocations at regular intervals. This platform serves as a controlled system for generating a real-space map of BCP fluctuations under variable confinement strain. Notably, we find that defects act as fluctuation hotspots, where local dynamics are substantially enhanced. We attribute this enhancement to two primary factors: (1) direct coupling of fluctuations to defect motion and (2) increased chain susceptibility near defect sites. Away from defects, the intensity of thermal fluctuations shows additional variation across the confined area, depending on both local strain and proximity to the sidewall boundaries. To explain these observations, we derive a free-energy model based on perturbations to the internal domain structure, which provides a predictive framework for mapping the fluctuation intensity. Finally, we leverage the improved time resolution of high-speed AFM to examine specific mechanisms for the formation and annihilation of confined dislocation pairs. Altogether, these findings serve to elucidate the role of confinement for mitigating disorder in BCP patterns.

EXPERIMENTAL SECTION

Samples were prepared on silicon wafer substrates (Virginia Semiconductor), cleaned by ultrasonication in toluene and then acetone, followed by rinsing with isopropanol. Wedge-shaped patterns were generated through electron-beam lithography using an FEI NanoSEM 230 with PMMA as the electron-beam resist. After development in methyl isobutyl ketone for 35 s, the patterned samples were rinsed extensively with isopropanol to prepare the PMMA mask. The mask patterns were then transferred to the silicon substrate with CF_4 and O_2 plasma dry etching, using a South Bay Technologies, Inc. RIE-2000. The resulting trenches had an opening angle of 5° and a depth of approximately 50 nm. The nanopatterned substrates were further cleaned with toluene and isopropanol to remove residual resist material. Polymer thin-films were then prepared by spin-casting 0.9 wt % solutions of PS-*b*-PMMA (77 kg/mol, 71 wt % PS, Polymer

https://doi.org/10.1021/acs.macromol.4c00638
Macromolecules 2024, 57, 7270−7279

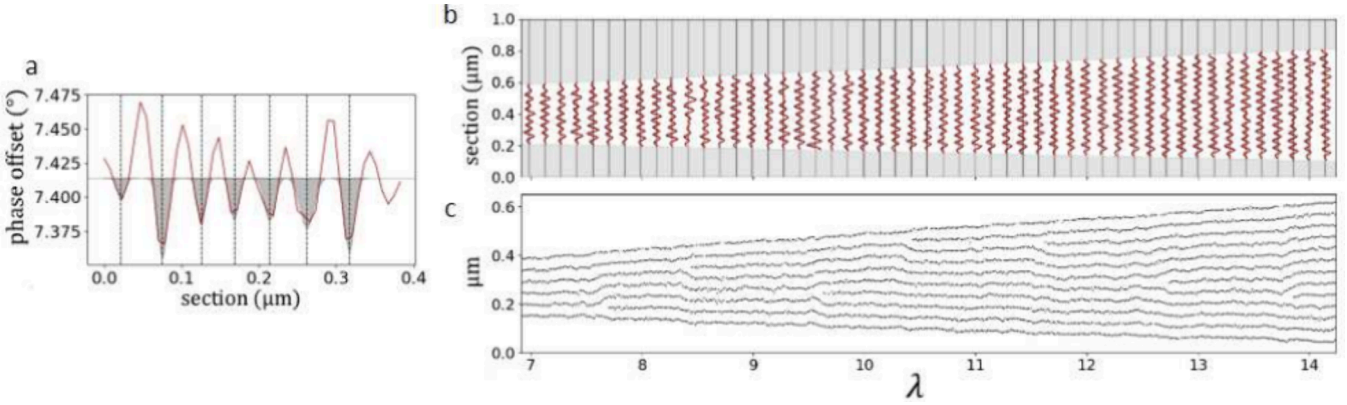

Figure 2. Analysis of domain positions. (a) Cross-section of the AFM phase signal showing alternating PS and PMMA domains. The peaks correspond to the PS matrix, and the valleys to the PMMA cylinders. The center position of each PMMA domain, indicated by the dashed vertical lines, is identified through Gaussian fitting (gray). (b) Applying this method along each pixel column generates a complete map of the domain structure. For clarity, only every tenth section is shown. (c) The resulting map of PMMA center positions.

Source) in toluene. The samples were preannealed for 1 h at 250 °C under an argon atmosphere to ensure polymer flow into the lithographic trenches.

High-speed tapping mode AFM imaging was performed with an Asylum Research Cypher ES Environmental AFM, using FS-1500 cantilevers with 1.5−2.0 MHz resonant frequency and a set point of 500 mV to prevent sample damage during scanning. The samples were heated *in situ* to 245 or 250 °C at a ramp rate of 1 °C s^{-1}. While annealing, a stream of argon gas was flowed through the sample chamber with an overpressure of 30−40 mbar to ensure an oxygen-free environment. Upon reaching the set point temperature, the cantilever resonance was redetermined prior to imaging. The samples were then imaged continuously with a line scan rate of 19.53 Hz with 512 × 256 pixel resolution over a 4 μm × 2 μm area, giving an overall imaging rate of 26.2 s per image.

The AFM phase images were processed and analyzed with custom Python code using the NumPy, SciPy, and Pandas packages.[33−35] In each image and for each pixel column, the center positions of the PMMA domains were determined through Gaussian fitting of lateral cross-sections across the width of trench. Individual features were then grouped together over time using K-means clustering to track domain dynamics. For this analysis, images were drift corrected by identifying a stationary dust particle to serve as a fiducial marker. Fluctuation intensities were determined from the standard deviation in lateral position at each point along each domain. Strain measurements of each domain i were calculated from the average interdomain distance from adjacent domains $i - 1$ and $i + 1$, except for edge domains where strain was measured from a single interdomain spacing. Space-filling two-dimensional (2D) strain and fluctuation maps were generated through linear interpolation from the measured data points taken along the PMMA domains.

RESULTS AND DISCUSSION

For our experiments, we examine the *in situ* dynamics of cylinder-forming poly(styrene-*block*-methyl methacrylate) (PS-*b*-PMMA) with a molecular weight of 77 kg/mol and 71 wt % PS. The equilibrium domain spacing is $d_0 = 45.5 \pm 2.9$ nm, as determined from the 2D Fourier transform of an image of unconfined polymer. To study the effects of confinement, we prepare wedge-shaped lithographic trenches with an opening angle $\theta = 5°$. Figure 1a shows an example AFM phase image of the confined BCP pattern. The polymer domains exhibit strong contrast, with PMMA cylinders appearing dark and the PS matrix appearing light. Outside the confining trench, the domains are oriented randomly, while within the trench the pattern preferentially aligns with the sidewalls. In the area immediately surrounding the trench, the film is locally depleted and is too thin to form the cylinder morphology, causing the surface to appear featureless.

Across the 4 μm wide image, the trench confinement width W steadily expands from approximately 320 to 670 nm, and the number of confined domains n correspondingly increases from 7 to 14. We note that n accounts for the two half-width wetting layers on either edge of the trench and is therefore one greater than the cylinder count. The value of n is discrete and changes discontinuously to minimize the confinement free energy per polymer chain F_c:

$$\frac{F_c(n, \lambda)}{F_0} = \frac{1}{3}\left(\left(\frac{\lambda}{n}\right)^2 + \frac{2n}{\lambda}\right) \quad (1)$$

where F_0 is the free energy of an unconfined chain, and λ is the dimensionless reduced width $\lambda = W/d_0$. In this expression, the first term reflects the elastic chain stretching energy, and the second term measures the interdomain surface tension.[18] Although originally derived for lamellar systems, this expression also generalizes to single layers of confined spheres or cylinders.[32,36]

A plot of free energy as a function of confinement width is shown in Figure 1b. Discontinuous changes in the free-energy minimum occur at regular intervals where $F_c(n, \lambda) = F_c(n + 1, \lambda)$, and these points correspond to dislocations where a new domain appears. During annealing, defects fluctuate about these equilibrium positions along the trench axis, particularly at larger trench widths where the free-energy landscape is shallower.[32] Defects are also able to migrate laterally back-and-forth across the trench width over relatively small energetic barriers.[32]

Between defect sites, the confined polymer stretches or compresses from its equilibrium spacing d_0 to accommodate the varying trench width. At each point along the trench, the average strain due to confinement is $\epsilon = (\lambda/n) - 1$. Within the wedges, this strain follows a sawtooth profile, as shown in Figure 1c, steadily increasing between dislocations and discontinuously dropping at the defect points. Because strain is distributed across domains, its magnitude decreases as the trench widens and more chains participate, bounded by peak values of $\pm 1/(2\lambda)$ at defect sites.[19] Altogether, this platform allows us to systematically control the strain environment for studying the dynamics of thermal fluctuations and pattern defects.

https://doi.org/10.1021/acs.macromol.4c00638
Macromolecules 2024, 57, 7270−7279

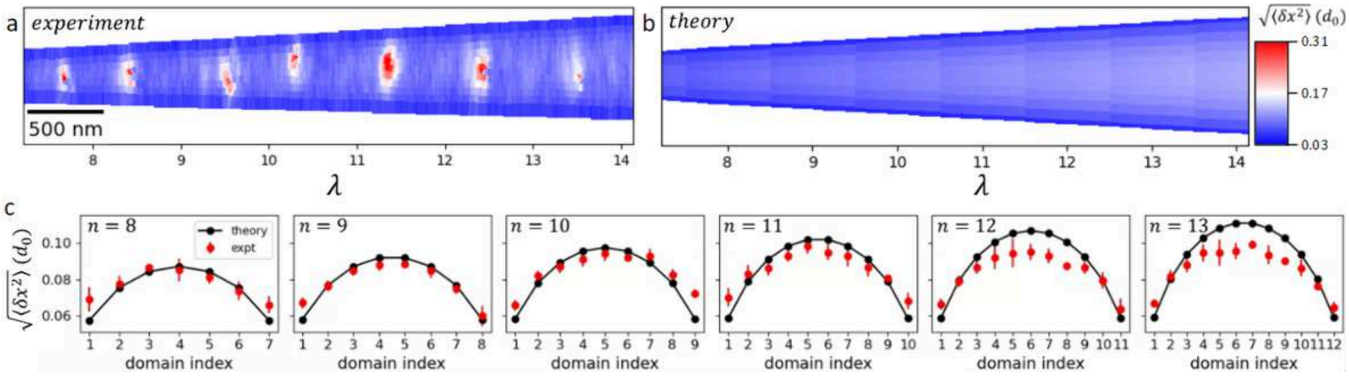

Figure 3. Fluctuation intensity maps. (a) Map of experimentally measured lateral fluctuations of PMMA center positions $\sqrt{\langle \delta x^2 \rangle}$ measured over 160 frames. Strong fluctuation enhancement is observed near defect positions. (b) Map of predicted fluctuation intensities determined from eq 6. Because defects are not included in the model, fluctuation hotspots at defect sites are not observed. (c) Cross-sections comparing experimental and theoretical fluctuations at commensurate trench widths, where $\lambda = n$, between the defect sites.

Mapping Thermal Fluctuations of the Block Copolymer Pattern. To record domain fluctuations, we continuously imaged confined patterns for periods of at least 1 h during *in situ* thermal annealing at 250 °C. This annealing temperature is above the glass transition to facilitate polymer mobility, but is well below the order−disorder transition to ensure strong domain segregation. Prior to imaging, samples were held at the annealing temperature for 15 min to ensure equilibration and imaging stability. An example movie of the fluctuating film is provided as Supporting Information (Video S1). For image analysis, we extract the cylinder positions by examining lateral cross-sections across the trench. The sections display alternating PS and PMMA domains, which appear as peaks and valleys, respectively, in the AFM phase signal (shown in Figure 2a), and each PMMA domain is fitted to a Gaussian profile to determine its central position. The fits provide subpixel lateral resolution, allowing us to identify the domain center positions with a precision of less than 1 nm. We then repeat this procedure across each of the 512 pixels along the trench (Figure 2b) to generate a complete spatial map of the domain structure (Figure 2c).

By applying this analysis to each image in the series, we can build a dynamic profile of the domain positions over time. The fluctuation intensity for a given confinement width and domain index is defined as the standard deviation $\sigma = \sqrt{\langle \delta x^2 \rangle}$ of that domain's lateral position, calculated over the imaging period. This measure is closely related to line placement roughness, which has a standard definition of $3\sigma^2$, although the variance is typically determined by averaging over space rather than time. Because each domain element is analyzed independently without spatial averaging, our approach provides a sensitive measure of spatial variations in fluctuation intensity.

Figure 3a shows the resulting fluctuation intensity map measured over a 70 min (160 frames) observation time scale. Notably, fluctuations are amplified around defect sites, where the pattern structure is locally perturbed. This enhancement partially results from motion of the defects themselves but also includes contributions from increased strain and enhanced chain mobility in the vicinity of defects, as discussed in detail below. Away from defects, we find additional spatial variation, depending on both local strain and proximity to the trench sidewalls. Domain fluctuations are strongest at the center of the trench and become increasingly damped approaching the edges. This pattern is maintained along the length of the trench, with a modest overall increase in fluctuation intensity as the trench widens.

Free-Energy Model of Fluctuations in Confined Block Copolymer. To understand these effects, we develop an analytic model to describe the thermal fluctuations of confined BCP films. For convenience, in the following derivation we express all length scales in units of d_0 and all energy scales in units of F_0. The confinement free energy described in eq 1 corresponds to the case where the confined domains are equally spaced, and strain is evenly distributed.[18] Under this description, the confined region may be divided along the center of any domain $1 \le i \le n - 1$ to form two subregions with widths λ_i and λ_{n-i}. Because strain is shared uniformly, the width of each subregion satisfies $\lambda/n = \lambda_i/i = \lambda_{n-i}/(n - i)$). The free energy per polymer chain of the original confined region is therefore equivalent to the sum of weighted contributions from the subregions:

$$F_c(n, \lambda) = \frac{i}{n} F_c(i, \lambda_i) + \frac{n - i}{n} F_c(n - i, \lambda_{n-i}) \tag{2}$$

To determine the energy associated with domain fluctuations, we consider the perturbative effect of a displacement x on the center position of domain i. We define the fluctuation energy ΔF_i as the energy penalty due to simultaneous expansion and contraction of the subregions:

$$F_c(n, \lambda) + \Delta F_i(n, \lambda, x) = \frac{i}{n} F_c(i, \lambda_i + x) + \frac{n - i}{n} F_c(n - i, \lambda_{n-i} - x) \tag{3}$$

This linear expression includes the implicit assumption that perturbations of one domain are accommodated by coherent displacements of the neighboring domains. Previous experiments have shown strong coherence across confined trenches, suggesting that it is reasonable to neglect the influence of higher-order fluctuations.[28] Solving for the fluctuation energy per chain, we obtain

$$\Delta F_i(n, \lambda, x) = \frac{1}{3n}\left[\left(\frac{1}{i} + \frac{1}{n - i}\right)x^2 + 2\left(\frac{i^2}{\lambda_i + x} + \frac{(n - i)^2}{\lambda_{n-i} - x} + \frac{n^2}{\lambda}\right)\right] \tag{4}$$

https://doi.org/10.1021/acs.macromol.4c00638
Macromolecules 2024, 57, 7270−7279

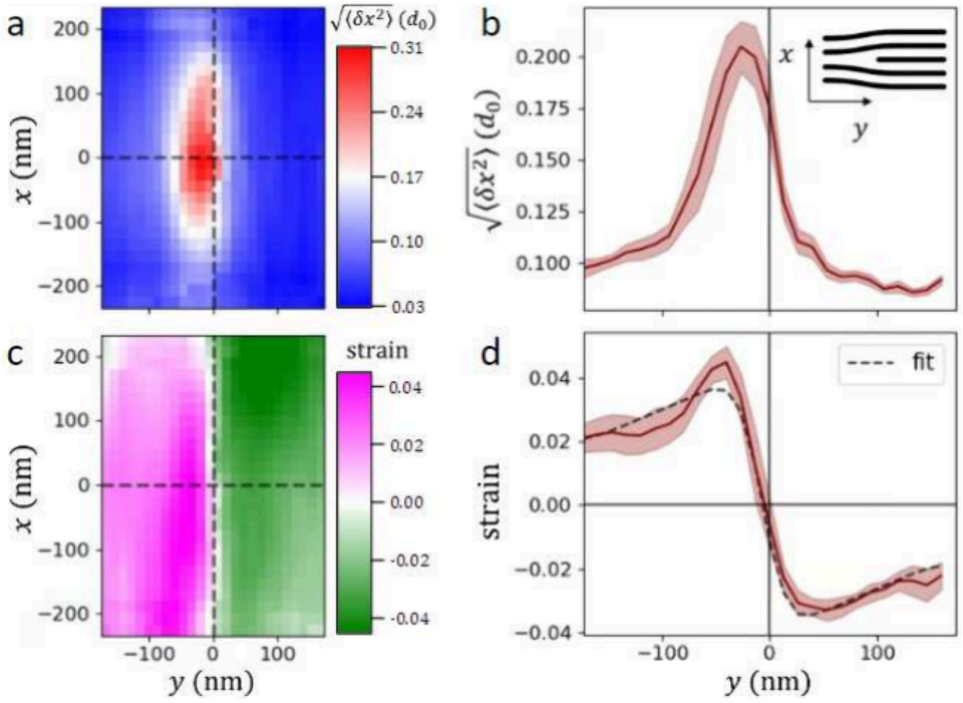

Figure 4. Fluctuation enhancement at defect sites. (a) Map of the mean fluctuation environment surrounding dislocations and (b) a horizontal cross-section showing the fluctuation intensity running through the defect core. (c) Map of pattern strain and (d) corresponding strain cross-section averaged over the same regions. The strain cross-section is fit as a sawtooth wave convolved with a Gaussian profile, which represents broadening from defect motion.

In accord with the fluctuation−dissipation theorem, the fluctuation intensity $\langle \delta x^2 \rangle$ integrated over the full power spectrum is related to the linear response of the system near equilibrium $\langle \delta x^2 \rangle = k_B T \xi$, where $k_B T$ is the thermal energy and ξ is the susceptibility, defined $\xi = (\partial^2 F/\partial x^2)^{-1}$. Using eq 4 to solve for the susceptibility of the i-th domain, we obtain

$$\langle \delta x^2 \rangle = \frac{3k_B T}{2m}\left[\frac{n}{i(n-i)} + 2\left(\frac{i^2}{(\lambda_i + x)^3} + \frac{(n-i)^2}{(\lambda_{n-i} - x)^3}\right)\right]^{-1} \quad (5)$$

where the constant m is the number of chains per domain. This term accounts for all chains that participate in domain fluctuations, including both direct participation and longer-range collective interactions. At equilibrium, $x = 0$ and (eq 5) simplifies to

$$\langle \delta x^2 \rangle = \frac{3k_B T}{2m}\left(1 + 2\left(\frac{n}{\lambda}\right)^3\right)^{-1}\left(\frac{i(n-i)}{n}\right) \quad (6)$$

The fluctuation intensity obtained in eq 6 reflects the product of three terms: a constant prefactor, the contribution of strain, and the positional dependence. The prefactor, with $k_B T$ expressed in units of F_0, includes the dependence on temperature and BCP composition. The strain term, which varies longitudinally in wedge-shaped trenches, describes the influence of the changing confinement width. Its value tends toward 1/3 as the trench widens and strain approaches zero. In our experiments, the strain term shows relatively minor variation, ranging from 0.28 in the most compressed regions (where $\epsilon \sim -0.08$) to 0.39 in the most extended regions (where $\epsilon \sim 0.08$).

Meanwhile, the positional term, which varies laterally, depends on the domain index i and is symmetric across the width of the trench. Fluctuations are suppressed in domains along the sidewalls, which act as fixed boundaries, relative to domains near the center of the trench where the local environment is more similar to unconfined BCP. In the limit of large n, this term approaches a value of 1 for edge domains ($i = 1, n - 1$) and diverges for central domains ($i \sim n/2$). We emphasize that this result represents a relaxation of the upper bound imposed by confinement and does not indicate a physical divergence of the fluctuation intensity. In general, the predictions of eq 6 are applicable in cases where confinement is the limiting factor, including narrow trenches or domains near sidewall boundaries. For wider trenches, the environment away from the sidewalls resembles bulk unconfined films where fluctuations are instead governed by intrinsic polymer properties, including the chain length and block segregation strength χ.[22,37]

From our model, Figure 3b shows a map of predicted fluctuation intensities with varying confinement width. In this map, the value of n is set as the number of confined cylinders at equilibrium according to eq 1. Although our model considers the effects of strain and confinement, it assumes that fluctuations represent linear perturbations from the equilibrium geometry. Defects are not included in this representation, and, as a consequence, the model does not exhibit the strong fluctuation enhancements observed experimentally in Figure 3a. Dislocations are nonequilibrium structures, introducing intrinsic strain that heightens the susceptibility of neighboring domains beyond the model prediction. The differences between the experimental and theoretical maps affirm the specific role of defects in enhancing fluctuations, as opposed to varying confinement strain from the wedge geometry.

Nonetheless, the model accurately captures fluctuation trends away from defect sites. As a comparison of our

https://doi.org/10.1021/acs.macromol.4c00638
Macromolecules 2024, 57, 7270−7279

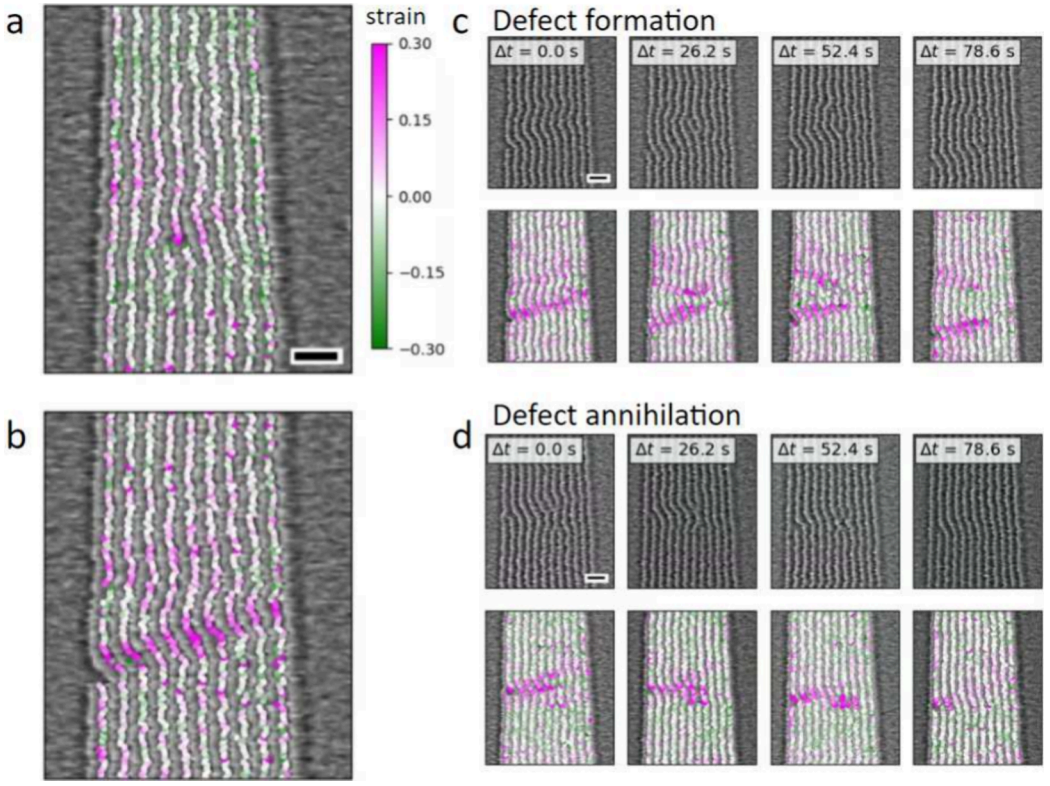

Figure 5. Defect dynamics and local strain. Comparison of the strain environments generated around (a) defects at equilibrium positions and (b) misplaced defects. PMMA domains in the AFM phase images are color-coded according to the interdomain strain. Pink indicates tensile strain, and green indicates compressive strain. (c) Time series showing pattern dynamics during a defect formation event. The upper plots show high-speed AFM phase images and the lower plots are labeled to show local strain. (d) Time series of the pattern evolution during defect annihilation. Defect healing results in well-ordered domains with minimal strain. Scale bars are 100 nm.

experimental and theoretical results, Figure 3c shows fluctuation intensity measurements in cross-sections at commensurate trench widths between the defect positions, i.e., where $\lambda = n$ and strain is zero. For this analysis, the experimental points are averaged over 5-pixel-wide sections. Each section exhibits a symmetric profile across the trench, with close agreement between experiment and theory. We note that the model includes only a single unknown parameter, the number of participating chains, m, which serves as an effective damping factor. By fitting, we obtain a global value of $m \sim 22$. This measured value is larger than the expected 5 to 6 chains per domain present in the sampled cross-sections, indicating that longer-range collective effects as well as interactions with the underlying BCP wetting layer may contribute to further damping the fluctuation intensity. Experimental fluctuations of domains adjacent to the trench sidewalls are also slightly enhanced over the model, potentially due to spatial variation of this chain damping parameter.

For sections with $n \geq 12$, measured fluctuations near the center of the trench are systematically reduced relative to the model prediction, indicating the transition from confinement-limited behavior to bulk-like dynamics. Previously reported phase field simulations have suggested that the influence of external confining fields extends roughly seven domains,[22] corresponding to $n \sim 14$ when there are two sidewall boundaries. Beyond this distance, fluctuations are expected to be indistinguishable from bulk-like modes.

Altogether, our result in eq 6 offers a quantitative framework for understanding the role of confinement in restricting pattern fluctuations. This picture aligns with previously reported empirical observations of confined BCP films, both from simulation[21,22] and experiment.[28] In unconfined films, structural perturbations of the BCP pattern are accommodated by surrounding domains which redistribute strain over a larger volume. Fluctuations of bulk lamellar BCP patterns have been demonstrated to include the contribution of coherent undulatory and peristaltic modes that extend across many layers.[11,28,38] Under confinement, however, the fixed sidewalls provide a stabilizing field that hinders the dynamics of neighboring domains and suppresses interdomain correlations.[22]

Fluctuations and Strain near Defect Sites. By stabilizing dislocations at specified locations, wedge-shaped trenches provide an additional opportunity for the controlled investigation of defect dynamics. Our analysis follows two approaches: first, examining the time-averaged influence of defects on local fluctuations, and, second, directly observing the time progression of dislocation formation and annihilation mechanisms. In each case, we leverage our real-space imaging to connect these nanoscale dynamics to the local strain environment.

To better understand how defects enhance local domain mobility, we consider the mean fluctuation environment surrounding defect sites. Figure 4a presents a map of fluctuation intensity aggregated over seven defects and averaged over 160 frames. Figure 4b shows the same measured intensity taken as a cross-section running through the dislocation core. The origin marks the time-averaged position of the dislocation cores, aligned with a consistent orientation as illustrated in the inset of Figure 4b. In Figures 4c,d, we show

https://doi.org/10.1021/acs.macromol.4c00638
Macromolecules 2024, 57, 7270−7279

strain and the corresponding strain cross-section averaged over the same defect regions and time period. Strain is determined from measurements of the interdomain spacing of real-space maps of the domain structure (as shown in Figure 2c). Within the trench, defects delineate a sharp crossover from tensile strain ($\epsilon > 0$) to compressive strain ($\epsilon < 0$) as the number of domains increases. The mean strain profile is a signature of the varying confinement width of the wedge-shaped trench. The model fit in Figure 4d shows a sawtooth wave representing the confinement strain, convolved with a Gaussian to account for the fluctuating positions of defect centers.

The fluctuation distribution in Figure 4a is anisotropic, primarily extending along the axis perpendicular to the striped BCP pattern. The shape of the distribution is partially influenced by motion of the defect center positions over the observation period and reflects the preference for lateral defect migration at equilibrium.[32] Fluctuations are coupled to defect motion as neighboring domains must shift to accommodate the moving dislocation core. However, the lateral span of the fluctuation enhancement extends several domains beyond the actual distribution of defect positions (see Figure S1). Perturbations originating at the defect spread laterally through the coherent bending of multiple domain stripes. Conversely, the fluctuation range along the cylinder axis shows minimal persistence and closely matches the distribution of defect positions (Figure S1). The resulting anisotropy is similar to fluctuations in smectic membranes, where elastic deformations propagate between layers.[39]

The fluctuation distribution is also asymmetric, with the peak centered ahead of the mean dislocation core position. This asymmetry results from the inherent dipolar structure of the dislocation strain field. From our view of the local strain, we see that the enhancement is localized to regions where the polymer is in tension and disappears where chains are under compression. The enhanced area also coincides with a pocket of locally amplified strain, where domains must distort to bend around the dislocation core. In this region of the strain cross-section, we measure increased peak tensile strain where fluctuations are amplified, roughly 25% greater than predicted from the confinement geometry alone. Overextended chains in the vicinity of defects have greater susceptibility to external perturbation and exhibit correspondingly enhanced fluctuations.

Real-Time Tracking of Defects and Strain. We gain further insight into the relationship between defect dynamics and their strain environment by directly tracking the structural evolution of the pattern en route to equilibrium. So far, we have focused on equilibrated trenches, where stabilized defects appear at regular intervals according to the confinement geometry. However, at early annealing times before the pattern has fully organized, we find additional defect structures that do not conform to this equilibrium configuration. These "destabilized" defects include misplaced dislocations that appear at positions far from their predicted equilibrium sites. Such defects may be distinguished through comparisons of the local strain field, as illustrated in Figures 5a,b, which show maps of the lateral strain overlaid on AFM phase images. The instantaneous local strain is displayed by color-coding the PMMA domains, with pink indicating tensile strain and green indicating compressive strain. In stabilized defects (Figure 5a), strain is concentrated at the branching point just above the dislocation core, whereas in destabilized defects (Figure 5b) strain extends as a band across the full 500 nm trench width. Cylinders bend to accommodate the misplaced dislocation, tilting relative to the trench axis. In the neighborhood of defects, we measure an interdomain strain as high as $\epsilon = 0.30$, substantially greater than the $\epsilon \sim \pm 0.08$ peak background strain expected from confinement. Stress is likely concentrated along the upper and lower edges of the band, where there is significant domain bending, rather than being distributed over the entire tilted region.

Tracking the pattern over time, we observe that strained domains near a destabilized defect are subject to large-amplitude fluctuations, forming ripples that drive restructuring of the BCP pattern. Figure 5c shows a montage of consecutive images with 26.2 s time resolution, with the top panels showing AFM phase images and the lower panels displaying the corresponding strain field. A full movie of this process is included as Supporting Information (Video S2). Over this time series, we observe spontaneous defect formation through branching of one of the strained cylinder domains. In the first panel, alongside the primary strain band that initiates at the dislocation, ripples in the domain structure form a fainter secondary distortion approximately 150 nm above the defect. In the following panel, a domain branching event along the secondary band results in the creation of a pair of new dislocations with opposing Burgers vectors. Defect formation is typically disfavored in systems far from the order−disorder transition, incurring energy penalties on the order of $100k_BT$.[23] In this case, however, the energetic cost is offset by partial stress relaxation of the original pattern. The resulting configuration exhibits improved domain alignment and an overall reduction in strain. Instead of spanning the entire trench width, strained domains are localized to shorter lines connecting the misplaced defects.

With continued scanning of the same region, we later observe an encounter between two misplaced defects with antiparallel orientation, as shown in Figure 5d. The opposing dislocations experience long-range attraction, mediated by their mutual strain field.[40] Because the defects are located in the same layer, they each travel parallel to the stripe pattern without disturbing the domain connectivity. This migration process, known as climb, proceeds through the incremental rearrangement of chains at the defect terminus and has a negligible free-energy barrier.[41] As the defects converge, strain initially intensifies in the space between them. Simulations of lamellar BCP predict that this disconnected stripe geometry is thermodynamically unstable and that the domains will fuse with no energetic barrier.[42] Indeed, the dislocations annihilate within a single frame, joining together to form a well-aligned pattern.

These examples demonstrate the capability of high-speed AFM for real-time imaging of BCP pattern dynamics and associated strain. The sequences shown in Figure 5 each occur over a period of less than 80 s, significantly shorter than the frame rate of traditional AFM imaging. Capturing these events reveals that pattern equilibration follows an undirected and circuitous path through the potential energy landscape. In this case, resolving the stress from a misplaced dislocation involves the creation and subsequent annihilation of new defect pairs. Topological constraints prohibit direct transformations of the pattern structure, necessitating the migration and interaction of defects.[43] These rearrangements are slow in strongly segregated BCPs, because block incompatibility hinders chain diffusion across domains. Simulations predict that healing of even simple defect structures follows nonelementary mecha-

https://doi.org/10.1021/acs.macromol.4c00638
Macromolecules 2024, 57, 7270−7279

nisms, involving multiple thermodynamic barriers associated with the rupture and reformation of domains.[12] This complex energy landscape presents a challenge for annealing DSA systems, as patterns often remain kinetically trapped in metastable defect states.

Controlling thermal fluctuations in BCPs is critical for lithographic applications, where nanofabrication requires eliminating defects while also adhering to precise roughness standards. However, managing fluctuations presents an apparent trade-off: while fluctuations can accelerate defect healing, they also increase roughness. Strategies to improve this roughness, such as increasing the block segregation strength χ, often hinder pattern alignment kinetics and elevate defectivity.[3] Conversely, raising the annealing temperature can enhance defect healing rates, but comes at the cost of increased roughness.[44]

Despite these challenges, our results suggest that graphoepitaxy can circumvent this trade-off. The external confinement field promotes alignment while simultaneously suppressing fluctuations. The effect is substantial, showing a roughly 2.2-fold reduction in $\langle \delta x^2 \rangle$ between edge and central cylinders. Because the improvement fades with distance from the boundary, its benefit will be most pronounced for the confinement of individual domains, such as used in hole-shrink processes.[45] Further optimization of pattern roughness is possible by applying confinement in combination with other methods, including the use of high-χ BCPs.

More broadly, the objectives of reducing defects and controlling roughness do not inherently conflict. Defect healing is kinetically limited, while fluctuations are thermodynamic. Indeed, we observe a mutual influence between defects and fluctuations that may be exploited to improve alignment kinetics. Defects perturb neighboring domains, generating local stress fields that enhance segmental motion, which in turn promotes defect migration and reconfiguration. In general, fluctuations facilitate exploration of the potential energy landscape needed for BCP equilibration and alignment. A staged annealing protocol involving high-temperature annealing to enhance fluctuations and eliminate defects followed by slow cooling through the glass transition to minimize fluctuations could potentially mitigate both factors. Furthermore, the targeted enhancement of fluctuations at defect sites could offer an alternative route for improving BCP order without increasing the overall film roughness. As one example, neutral random copolymer additives have been shown to preferentially concentrate at strained defect sites, where they promote rapid defect annihilation by locally mediating the interblock interaction.[46] Altogether, direct observations of BCP dynamics refine our fundamental understanding of the interplay between defects and fluctuations and facilitate the development of new nanofabrication strategies.

CONCLUSION

Despite significant progress in the development of DSA for guiding the organization of nanoscale patterns, industrial applications remain limited by residual structural disorder. Defects and line roughness arise from dynamics that take place during polymer processing and annealing. Realizing the promise of DSA will therefore require improved measurement and understanding of BCP kinetics throughout the assembly process. In this study, we have demonstrated the utility of high-speed AFM for directly visualizing the interplay of fluctuations, strain, and defects in real space and time during thermal annealing. We apply these measurements to construct a spatial map of the fluctuation intensity of confined BCP domains, revealing strong fluctuation enhancement at defect sites. Our observations are supported by the development of an analytic free-energy model for predicting the magnitude of thermal fluctuations under confinement. Looking ahead, we envision extending these methods to examine a broader range of BCP systems and processing conditions, such as solvent vapor annealing, where chain dynamics and interactions are mediated by the solvent. Overall, this combined experimental and theoretical approach takes a critical step toward the goal of preparing perfected, defect-free BCP patterns.

ASSOCIATED CONTENT

Supporting Information

The Supporting Information is available free of charge at https://pubs.acs.org/doi/10.1021/acs.macromol.4c00638.

S1: Analysis of defect distributions (PDF)

Video S1: high-speed AFM movie showing pattern fluctuations, measured at 250 °C (MP4)

Video S2: high-speed AFM movie tracking defect healing dynamics alongside a map of pattern strain, measured at 245 °C (MP4)

AUTHOR INFORMATION

Corresponding Author

Steven J. Sibener − *Department of Chemistry and The James Franck Institute, The University of Chicago, Chicago, Illinois 60637, United States;* orcid.org/0000-0002-5298-5484; Phone: 773-702-7193; Email: s-sibener@uchicago.edu

Authors

Julia G. Murphy − *Department of Chemistry and The James Franck Institute, The University of Chicago, Chicago, Illinois 60637, United States;* orcid.org/0000-0001-6334-559X

Jonathan G. Raybin − *Department of Chemistry and The James Franck Institute, The University of Chicago, Chicago, Illinois 60637, United States*

Complete contact information is available at: https://pubs.acs.org/10.1021/acs.macromol.4c00638

Author Contributions

J.G.M. and J.G.R. contributed equally to this work.

Notes

The authors declare no competing financial interest.

ACKNOWLEDGMENTS

This work was supported by the U.S. Department of Commerce, National Institute of Standards and Technology as part of the Center for Hierarchical Materials Design (CHiMaD), under Award No. 70NANB19H005. J.G.M. and S.J.S. acknowledge support from the National Science Foundation Grants CHE-2313365 and CHE-1900188, including an NSF Alliances for Graduate Education and Professoriate supplement. We also thank the Advanced Materials for Energy-Water Systems (AMEWS) Center, an Energy Frontier Research Center funded by the US Department of Energy, Office of Science, Basic Energy Sciences. AFM measurements and sample preparation were supported by the NSF Materials Research Science and Engineering Center (MRSEC) at the University of Chicago, Grant No. NSF-DMR-2011854.

REFERENCES

(1) Stoykovich, M. P.; Kang, H.; Daoulas, K. C.; Liu, G.; Liu, C.-C.; de Pablo, J. J.; Müller, M.; Nealey, P. F. Directed Self-Assembly of Block Copolymers for Nanolithography: Fabrication of Isolated Features and Essential Integrated Circuit Geometries. *ACS Nano* **2007**, *1*, 168−175.

(2) Bates, C. M.; Maher, M. J.; Janes, D. W.; Ellison, C. J.; Willson, C. G. Block Copolymer Lithography. *Macromolecules* **2014**, *47*, 2−12.

(3) Chen, Y.; Xiong, S. Directed self-assembly of block copolymers for sub-10 nm fabrication. *International Journal of Extreme Manufacturing* **2020**, *2*, 032006.

(4) Jeong, J. W.; Park, W. I.; Kim, M.-J.; Ross, C. A.; Jung, Y. S. Highly Tunable Self-Assembled Nanostructures from a Poly(2-vinylpyridine-b-dimethylsiloxane) Block Copolymer. *Nano Lett.* **2011**, *11*, 4095−4101.

(5) Sinturel, C.; Bates, F. S.; Hillmyer, M. A. High χ−Low N Block Polymers: How Far Can We Go? *ACS Macro Lett.* **2015**, *4*, 1044−1050.

(6) Hur, Y. H.; Song, S. W.; Kim, J. M.; Park, W. I.; Kim, K. H.; Kim, Y.; Jung, Y. S. Thermodynamic and Kinetic Tuning of Block Copolymer Based on Random Copolymerization for High-Quality Sub-6 nm Pattern Formation. *Adv. Funct. Mater.* **2018**, *28*, 1800765.

(7) Li, W.; Müller, M. Directed self-assembly of block copolymers by chemical or topographical guiding patterns: Optimizing molecular architecture, thin-film properties, and kinetics. *Prog. Polym. Sci.* **2016**, *54*−*55*, 47−75.

(8) Liu, C.-C.; Thode, C. J.; Rincon Delgadillo, P. A.; Craig, G. S. W.; Nealey, P. F.; Gronheid, R. Towards an all-track 300 mm process for directed self-assembly. *J. Vac. Sci. Technol. B* **2011**, *29*, 06F203.

(9) Delgadillo, P. A. R.; Thode, C. J.; Nealey, P. F.; Gronheid, R.; Wu, H.; Cao, Y.; Neisser, M.; Somervell, M. H.; Nafus, K. Implementation of a chemo-epitaxy flow for directed self-assembly on 300-mm wafer processing equipment. *Journal of Micro/Nanolithography, MEMS, and MOEMS* **2012**, *11*, 031302.

(10) Bosse, A. W.; Lin, E. K.; Jones, R. L.; Karim, A. Interfacial fluctuations in an ideal block copolymer resist. *Soft Matter* **2009**, *5*, 4266−4271.

(11) Ruiz, R.; Wan, L.; Lopez, R.; Albrecht, T. R. Line Roughness in Lamellae-Forming Block Copolymer Films. *Macromolecules* **2017**, *50*, 1037−1046.

(12) Hur, S.-M.; Thapar, V.; Ramırez-Hernández, A.; Nealey, P. F.; de Pablo, J. J. Defect Annihilation Pathways in Directed Assembly of Lamellar Block Copolymer Thin Films. *ACS Nano* **2018**, *12*, 9974−9981.

(13) Liu, C.-C.; Franke, E.; Mignot, Y.; Xie, R.; Yeung, C. W.; Zhang, J.; Chi, C.; Zhang, C.; Farrell, R.; Lai, K.; Tsai, H.; Felix, N.; Corliss, D. Directed self-assembly of block copolymers for 7 nanometre FinFET technology and beyond. *Nature Electronics* **2018**, *1*, 562−569.

(14) Stoykovich, M. P.; Müller, M.; Kim, S. O.; Solak, H. H.; Edwards, E. W.; de Pablo, J. J.; Nealey, P. F. Directed Assembly of Block Copolymer Blends into Nonregular Device-Oriented Structures. *Science* **2005**, *308*, 1442−1446.

(15) Chang, J.-B.; Choi, H. K.; Hannon, A. F.; Alexander-Katz, A.; Ross, C. A.; Berggren, K. K. Design rules for self-assembled block copolymer patterns using tiled templates. *Nat. Commun.* **2014**, *5*, 3305.

(16) Segalman, R. A.; Yokoyama, H.; Kramer, E. J. Graphoepitaxy of Spherical Domain Block Copolymer Films. *Adv. Mater.* **2001**, *13*, 1152−1155.

(17) Sundrani, D.; Darling, S. B.; Sibener, S. J. Guiding Polymers to Perfection: Macroscopic Alignment of Nanoscale Domains. *Nano Lett.* **2004**, *4*, 273−276.

(18) Turner, M. S. Equilibrium properties of a diblock copolymer lamellar phase confined between flat plates. *Phys. Rev. Lett.* **1992**, *69*, 1788−1791.

(19) Walton, D. G.; Kellogg, G. J.; Mayes, A. M.; Lambooy, P.; Russell, T. P. A Free Energy Model for Confined Diblock Copolymers. *Macromolecules* **1994**, *27*, 6225−6228.

(20) Semenov, A. N. Theory of block copolymer interfaces in the strong segregation limit. *Macromolecules* **1993**, *26*, 6617−6621.

(21) Geisinger, T.; Müller, M.; Binder, K. Symmetric diblock copolymers in thin films. II. Comparison of profiles between self-consistent field calculations and Monte Carlo simulations. *J. Chem. Phys.* **1999**, *111*, 5251−5258.

(22) Bosse, A. W. Effects of segregation strength and an external field on the thermal line edge and line width roughness spectra of a diblock copolymer resist. *J. Vac. Sci. Technol. B* **2011**, *29*, 031803.

(23) Li, W.; Müller, M. Defects in the Self-Assembly of Block Copolymers and Their Relevance for Directed Self-Assembly. *Annu. Rev. Chem. Biomol. Eng.* **2015**, *6*, 187−216.

(24) Shelton, C. K.; Epps, T. H. Block copolymer thin films: Characterizing nanostructure evolution with in situ X-ray and neutron scattering. *Polymer* **2016**, *105*, 545−561.

(25) Sunday, D. F.; Kline, R. J. In *Directed Self-assembly of Block Co-polymers for Nano-manufacturing*; Gronheid, R., Nealey, P., Eds.; Woodhead Publishing Series in Electronic and Optical Materials; Woodhead Publishing: 2015; pp 171−197.

(26) Sunday, D. F.; Ren, J.; Liman, C. D.; Williamson, L. D.; Gronheid, R.; Nealey, P. F.; Kline, R. J. Characterizing Patterned Block Copolymer Thin Films with Soft X-rays. *ACS Appl. Mater. Interfaces* **2017**, *9*, 31325−31334.

(27) Murphy, J. G.; Raybin, J. G.; Sibener, S. J. Correlating polymer structure, dynamics, and function with atomic force microscopy. *J. Polym. Sci.* **2022**, *60*, 1042−1058.

(28) Raybin, J. G.; Murphy, J. G.; Dolejsi, M.; Sibener, S. J. Direct Imaging of Interfacial Fluctuations in Confined Block Copolymer with in Situ Slow-Scan-Disabled Atomic Force Microscopy. *ACS Nano* **2019**, *13*, 11741−11752.

(29) Raybin, J.; Ren, J.; Chen, X.; Gronheid, R.; Nealey, P. F.; Sibener, S. J. Real-Time Atomic Force Microscopy Imaging of Block Copolymer Directed Self Assembly. *Nano Lett.* **2017**, *17*, 7717−7723.

(30) Chandra, A.; Nakatani, R.; Uchiyama, T.; Seino, Y.; Sato, H.; Kasahara, Y.; Azuma, T.; Hayakawa, T. Direct In Situ Observation of the Early-Stage Disorder-Order Evolution of Perpendicular Lamellae in Thermally Annealed High-χ Block Copolymer Thin Films. *Advanced Materials Interfaces* **2019**, *6*, 1801401.

(31) Murphy, J. G.; Raybin, J. G.; Ansay, G. E.; Sibener, S. J. Spatiotemporal Mapping of Hole Nucleation and Growth during Block Copolymer Terracing with High-Speed Atomic Force Microscopy. *ACS Nano* **2023**, *17*, 5644−5652.

(32) Tong, Q.; Zheng, Q.; Sibener, S. J. Alignment and Structural Evolution of Cylinder-Forming Diblock Copolymer Thin Films in Patterned Tapered-Width Nanochannels. *Macromolecules* **2014**, *47*, 4236−4242.

(33) Harris, C. R.; et al. Array programming with NumPy. *Nature* **2020**, *585*, 357−362.

(34) Virtanen, P.; et al. SciPy 1.0: Fundamental Algorithms for Scientific Computing in Python. *Nat. Methods* **2020**, *17*, 261−272.

(35) McKinney, W. Data Structures for Statistical Computing in Python. *Proceedings of the 9th Python in Science Conference* **2010**, 56−61.

(36) Cheng, J. Y.; Mayes, A. M.; Ross, C. A. Nanostructure engineering by templated self-assembly of block copolymers. *Nat. Mater.* **2004**, *3*, 823−828.

(37) Bosse, A. W. Phase-Field Simulation of Long-Wavelength Line Edge Roughness in Diblock Copolymer Resists. *Macromol. Theory Simul.* **2010**, *19*, 399−406.

(38) Srinivas, G.; Swope, W. C.; Pitera, J. W. Interfacial Fluctuations of Block Copolymers: A Coarse-Grain Molecular Dynamics Simulation Study. *J. Phys. Chem. B* **2007**, *111*, 13734−13742.

(39) de Jeu, W. H.; Ostrovskii, B. I.; Shalaginov, A. N. Structure and fluctuations of smectic membranes. *Rev. Mod. Phys.* **2003**, *75*, 181−235.

(40) Li, W.; Müller, M. Thermodynamics and Kinetics of Defect Motion and Annihilation in the Self-Assembly of Lamellar Diblock Copolymers. *Macromolecules* **2016**, *49*, 6126−6138.

https://doi.org/10.1021/acs.macromol.4c00638
Macromolecules 2024, 57, 7270−7279

(41) Tong, Q.; Sibener, S. J. Visualization of Individual Defect Mobility and Annihilation within Cylinder-Forming Diblock Copolymer Thin Films on Nanopatterned Substrates. *Macromolecules* **2013**, *46*, 8538−8544.
(42) Li, W.; Nealey, P. F.; de Pablo, J. J.; Müller, M. Defect Removal in the Course of Directed Self-Assembly is Facilitated in the Vicinity of the Order-Disorder Transition. *Phys. Rev. Lett.* **2014**, *113*, 168301.
(43) Harrison, C.; Adamson, D. H.; Cheng, Z.; Sebastian, J. M.; Sethuraman, S.; Huse, D. A.; Register, R. A.; Chaikin, P. M. Mechanisms of Ordering in Striped Patterns. *Science* **2000**, *290*, 1558−1560.
(44) Pathangi, H.; et al. Defect mitigation and root cause studies in 14 nm half-pitch chemo-epitaxy directed self-assembly LiNe flow. *J. Micro/Nanolith. MEMS MOEMS* **2015**, *9423*, 94230M.
(45) Younkin, T. R.; Gronheid, R.; Delgadillo, P. R.; Chan, B. T.; Vandenbroeck, N.; Demuynck, S.; Romo-Negreira, A.; Parnell, D.; Nafus, K.; Tahara, S.; Somervell, M. Progress in directed self-assembly hole shrink applications. *Advances in Resist Materials and Processing Technology XXX* **2013**, 143−153.
(46) Kim, B. H.; Park, S. J.; Jin, H. M.; Kim, J. Y.; Son, S.-W.; Kim, M.-H.; Koo, C. M.; Shin, J.; Kim, J. U.; Kim, S. O. Anomalous Rapid Defect Annihilation in Self-Assembled Nanopatterns by Defect Melting. *Nano Lett.* **2015**, *15*, 1190−1196.

https://doi.org/10.1021/acs.macromol.4c00638
Macromolecules 2024, 57, 7270−7279